11-1-2010

Automated Classification of Breast Pathology using Local Measures of Broadband Reflectance

Ashley M. Laughney
Dartmouth College

Venkataramanan Krishnaswamy
Dartmouth College

Pilar Beatriz Garcia-Allende
University de Cantabria

Olga M. Conde
University de Cantabria

Wendy A. Wells
Dartmouth College

See next page for additional authors

Automated classification of breast pathology using local measures of broadband reflectance

Ashley M. Laughney
Venkataramanan Krishnaswamy
Dartmouth College
Thayer School of Engineering
8000 Cummings Hall
Hanover, New Hampshire 03755

Pilar Beatriz Garcia-Allende
University of Cantabria
Photonics Engineering Group
Avda. de los Castros S/N
Santander 39005, Spain
and
Imperial College London
Department of Surgery and Cancer
Exhibition Road
London SW7 2AZ, United Kingdom

Olga M. Conde
University of Cantabria
Photonics Engineering Group
Avda. de los Castros S/N
Santander 39005, Spain

Wendy A. Wells
Dartmouth-Hitchcock Medical Center
Department of Pathology
1 Medical Center Drive
Lebanon, New Hampshire 03756

Keith D. Paulsen
Brian W. Pogue
Dartmouth College
Thayer School of Engineering
8000 Cummings Hall
Hanover, New Hampshire 03755

Abstract. We demonstrate that morphological features pertinent to a tissue's pathology may be ascertained from localized measures of broadband reflectance, with a mesoscopic resolution (100-μm lateral spot size) that permits scanning of an entire margin for residual disease. The technical aspects and optimization of a *k*-nearest neighbor classifier for automated diagnosis of pathologies are presented, and its efficacy is validated in 29 breast tissue specimens. When discriminating between benign and malignant pathologies, a sensitivity and specificity of 91 and 77% was achieved. Furthermore, detailed subtissue-type analysis was performed to consider how diverse pathologies influence scattering response and overall classification efficacy. The increased sensitivity of this technique may render it useful to guide the surgeon or pathologist where to sample pathology for microscopic assessment. [DOI: 10.1117/1.3516594]

Keywords: vis-NIR spectroscopy; backscattering; tissues; biomedical optics.

Paper 10236RR received May 2, 2010; revised manuscript received Sep. 26, 2010; accepted for publication Oct. 4, 2010; published online Dec. 30, 2010.

1 Introduction

Breast-conserving therapy (BCT), which includes local excision and radiation treatment to the breast, has been the standard of care for early invasive breast cancers (stages I and II) since Fisher and Veronisi demonstrated that BCT is equally safe and effective as mastectomy for most patients when surgical margins are clear of residual disease.[1] However, the number of patients with residual disease at or near the cut edge of their primary surgical specimen ranges from 5 to 82%, with the majority of studies indicating positive margins in 20–40% of patients.[2] This high variability indicates that surgical margin assessment lacks standardization, despite its importance to a patient's long-term prognosis. In a large retrospective analysis of frozen sections by Rogers et al.[3] and Laucirica,[4] diagnostic errors related to intraoperative evaluation of involved margins were attributed to interpretation (57%), microscopic sampling (24%), gross sampling (9.5%), and lack of communication between pathologist and surgeon (9.5%). Effective margin assessment evidently requires a wide-field imaging technology with resolution sensitive to diagnostically differentiating volumes of tissue and automated interpretation of results. To reduce sampling error, a broadband reflectance imaging system was designed to provide localized measures of spectroscopic information at a resolution that permitted wide-field scanning of a surgical specimen.[5] To address interpretation error,scattering maps were associated with diagnostically relevant pathologies using an automated *k*-nearest neighbor (*k*-NN) classifier.[6] The effective illumination volume of the imaging system (100-μm lateral resolution) was specifically chosen to optimize direct sampling of elastic scattering

Address all correspondence to: Ashley M. Laughney, Dartmouth College, Thayer School of Engineering, 8000 Cummings Hall, Hanover, New Hampshire 03755; Tel: 802-343-8737; E-mail: ashley.laughney@dartmouth.edu

1083-3668/2010/15(6)/066019/12/$25.00 © 2010 SPIE

features, which are highly sensitive to tissue architectural changes at the cellular and subcellular levels.[7,8] These scattering features are quite relevant to the tissue parameters a pathologist would address during microscopic assessment of a surgical specimen. The ability of the *k*-NN classifier to accurately detect morphological variations in tissue was first demonstrated in a mouse pancreas model,[5,6] and here its ability to discriminate pathologies was demonstrated in human breast tissues. The morphology of pancreas and breast tumors are fundamentally different; the former is often dominated by abundant, sclerotic, malignant stroma while the latter usually has a more prominent malignant epithelial component.

A positive surgical margin is a major predictor of local recurrence;[9–12] consequently the standard of care at Dartmouth-Hitchcock Medical Center (DHMC) for more than seven years has been to reexcise a margin if invasive tumor is "at" that margin and/or if ductal carcinoma *in situ* (DCIS) is <0.1 cm from the margin (WAW). The poor prognosis associated with positive margins necessitates this standard of care, despite the well-documented psychological effects and suboptimal cosmetic results following repeated surgery.[13,14] Current modalities of intraoperative margin assessment include gross examination of the specimen, frozen section analysis (FSA), and touch preparation cytology.[4,15,16] Each has its limitations: gross evaluation of the specimen does not reflect the microscopic margin status;[15] FSA often results in severe histological artifacts (particularly in the breast because of its high adipose content) and requires substantial processing time (~30 min, requiring immediate access to a cryostat and pathologist);[2,16] and touch preparation cytology is undesirable because of its inability to localize a "positive" measure.[15] New techniques for margin delineation must be simple, rapid, and nondisruptive to surgical workflow. Intra-operative assessment of sentinel lymph node(s) could also have significant clinical impact during BCT, as recently demonstrated by Austwick.[17] Principle components extracted from elastic scattering spectra were classified according to pathology and the need for axial lymph node dissection was determined with a sensitivity and specificity of 69% and 96% respectively.[17]

Spectroscopy methods have been studied extensively as diagnostic tools for identifying residual disease in involved surgical margins; particularly, fluorescence, diffuse reflectance, and Raman spectroscopy have been used to provide biochemical information, and scattering spectroscopy has been used to provide ultrastructural information about a tissue.[18–23] The effective illumination volume determines the transport model and, consequently, the type of information obtained because measures are averaged over different tissue volumes likely in different physiological states. Techniques that probe larger volumes of tissue and diffuse light rely on the assumption that ultrastructural malignant transformations provide disease-specific contrast in volume-averaged measures, but sensitivity of the measurement to specific features of the tissue is not yet clear. Backman et al.[7,24] and Perelman et al.[8] demonstrated that wavelength-dependent variations in the intensity of singly backscattered photons were sensitive to nuclear enlargement, pleomorphism, crowding, and hyperchromatism.[7,8,24] Using light-scattering spectroscopy (LSS), they observed alterations in the size and number density of epithelia in Barrett's esophagus, the bladder, oral cavity, and colon.[25–28] Georgakoudi augmented LSS with diffuse reflectance spectroscopy and fluorescence spectroscopy (trimodal spectroscopy) to discriminate between dysplasia or cancerous and normal oral tissues, achieving a sensitivity and specificity of 96%.[28] Keller et al.,[29] Breslin et al.,[30] Palmer et al.,[31] and Zhu et al.,[32] combined diffuse reflectance with fluorescence spectroscopy to discriminate between benign and malignant breast tissues, achieving a sensitivity: specificity of 70.0%:91.7% and 78%:99%, respectively. More recently, Keller et al.[29] developed a Monte Carlo inverse model to generate chromophore and scattering maps from visible–near-infrared diffuse reflectance spectra. When applied to 55 surgical margins, a multivariate predictive model discriminated between positive and negative breast tissue margins up to 2 mm in depth, with a sensitivity and specificity of 79 and 67%, respectively.[33] Amelink, Sterenborg, Amelink et al., and van Veen et al.[34–36] developed differential path-length spectroscopy to determine local optical properties of breast tissue *in vivo* using a fiber-optic needle probe with optimized source-detector separation. The sensing depth of the probe was specifically limited to 240 μm, so that the photon pathlength was independent of wavelength, allowing straightforward interpretation of the measured signal in terms of absorption and scattering.[34–36]

The confocal measurement geometry employed here was designed to minimize multiple scattering and absorption effects; therefore, the analysis focuses only on the spectral response of photons experiencing few scattering events and their value to classification. The lateral resolution was fixed at 100 μm (approximately one mean scattering pathlength in tissue) because this obstructed multiply scattered light.[5,37–39] A strong periodicity in wavelength related to the size of scattering centers was not observed in localized tissue spectra because of the tissue's broad particle size distribution and because the system does not exclusively look at single scattering events. However, extracted scattering features in this mesoscopic volume demonstrate sensitivity to the tissue parameters a pathologist would address during microscopic assessment of a surgical specimen. Scattering measures are more robust and localized as compared to biochemical parameters, which tend to be diffuse, transient, and significantly different *in vitro* as compared to *in vivo*. Additionally, scattering parameters have not been evaluated sufficiently in a waveband that avoids coupling with absorption. A *k*-NN algorithm automated classification of spectral measures according to tissue pathology and was employed to guide the pathologist or surgeon where to look when evaluating involved surgical margins. The *k*-NN classifier was selected because it is simple, nonparametric, robust, has real-time capabilities, and good performance for optimal values of *k*.

2 Materials and Methods

2.1 *Localized Reflectance Spectroscopy*

Fresh breast tissue specimens were imaged in a custom-built microsampling reflectance spectral imaging system.[5] This system employs a quasi-confocal illumination and detection (510–785 nm) to constrain the overlapping illumination and detection spot sizes to within approximately one scattering distance in tissue (~100 μm in the visible). A complete description of this imaging system can be found in a previous study.[5] Sampling in this mesoscopic regime allows the use of simple

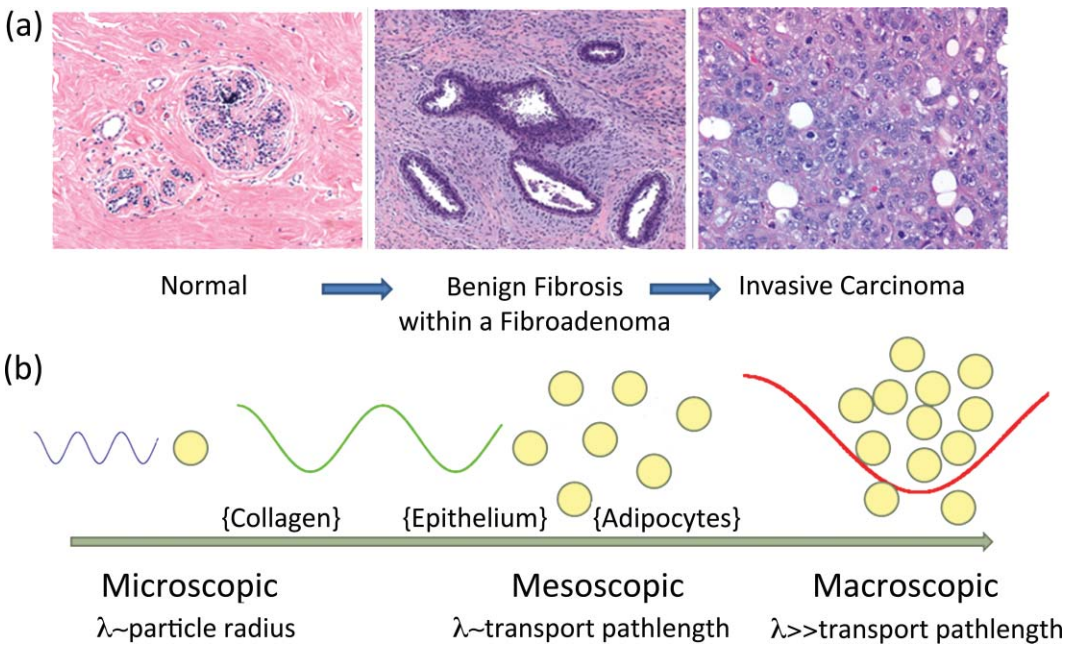

Fig. 1 (a) Representative H&E sections of breast tissue illustrating morphological features characteristics of distinct diagnostic categories in the breast and (b) illustrative relationship between radiation transport length scales and the primary scattering centers in breast tissue.

empirical models to describe the light transport (Fig. 1). For the short pathlengths involved and for typical values of absorption and scattering in tissue, the measured spectral response is proportional to the reduced scattering coefficient, $\mu s'$. In regions where significant local absorption is encountered, a Beer's law–type attenuation factor is used to correct for the effects of absorption.[5,37–39] Each tissue sample was mounted on a glass slide and surveyed across the illumination-detection path using a motorized translational stage. Each measurement took ~2 h, and during scanning, the sample was hydrated with a phosphate buffer solution. Trace background reflections from the optical system were acquired (R_{bkgrd}) and subtracted from measured spectra, and the data were normalized to the instrumental spectral response ($R_{\text{Spectralon}}$) of the system using a Spectralon reference (Labsphere, Inc., North Sutton, New Hampshire), as follows:

$$R(\lambda) = \frac{R_{\text{acquired}}(\lambda) - R_{\text{bkgrd}}(\lambda)}{R_{\text{Spectralon}}(\lambda) - R_{\text{bkgrd}}(\lambda)}. \quad (1)$$

Referencing to Spectralon also permitted direct comparison between tissue samples and provided a daily calibration.

An empirical approximation to Mie theory was used to describe the measured reflectance spectrum, $R(\lambda)$, from a volume-averaged region of tissue.[40] Additionally, a Beer's Law attenuation factor is required to correct for the presence of significant local absorption by hemoglobin,

$$R(\lambda) = A\lambda^{-b} \exp^{-\Gamma * [\text{Hb}_\text{T}]\{\text{StO}_2 * \varepsilon_{\text{HbO}_2}(\lambda) + (1-\text{StO}_2) * \varepsilon_{\text{Hb}}(\lambda)\}}. \quad (2)$$

Parameters A and b are scattering amplitude and scattering power, respectively. Both depend on the size and number density of scattering centers in the volume of interrogated tissue, thereby reflecting variations in breast tissue morphology.[41–43] Γ refers to the mean optical pathlength (dependent on the illumination and detection geometry), parameter $[Hb_T]$ is the total hemoglobin concentration, parameter StO_2 is the oxygen saturation factor (ratio of oxygenated to total hemoglobin), and ε_{HbO_2} and ε_{Hb} refer to the molar extinction coefficients of these two chromophores respectively (Oregon Medical Laser Center Database[44]). Oxygenated and deoxygenated hemoglobin were the dominant tissue chromophores encountered in the measured waveband. Measured reflectance spectra were fit to this model using a nonlinear least-squares solver to obtain estimates of scattering amplitude and scattering power relative to Spectralon. A measure of average scatter irradiance, I_{avg}, was calculated by integrating the reflectance spectrum over a waveband that avoids the hemoglobin absorption peaks (620:785 nm). Scattering parameters were then microscopically correlated to morphological features identified by a pathologist (WAW) on hematoxylin and eosin (H&E) stained sections of the tissue, cut in the exact same geometry as imaged *in situ*.

2.2 *Breast Tissue Surgical Specimens*

All studies were completed based on a protocol approved by the Committee for the Protection of Human Subjects, Institutional Review Board at Dartmouth. Fresh breast tissue was obtained directly from the Department of Pathology at DHMC from patients who had given informed consent to allow this use of their tissue. Samples were procured during conservative surgery or breast-reduction surgery and only provided if there was tissue in excess of that required to make a clinical diagnosis. Tissue samples were 1–2 cm^2 with a thickness of about 3–5 mm. Samples were imaged within 12 h of surgery, and in the case of delay, the tissue was stored in a 4°C refrigerator and hydrated with a phosphate buffer solution. Immediately following imaging, each sample was placed in 10% formalin and processed for histology (paraffin embedded, sectioned to 4 μm, and stained with H&E). A total of 35 tissue specimens were imaged; 6 were rejected from analysis due to a low signal-to-noise ratio and/or poor histological processing (both a consequence of highly fatty tissue). In the remaining 29 tissue samples, 48 regions of interest (ROI)

Table 1 Distribution of the sample population according to tissue type and subtype.

Tissue Type and Subtype	No. ROI	No. Spectra
Total Not Malignant	**25**	**36,979**
Normal Epithelia and Stroma	21	31,226
Benign Epithelia and Stroma	3	5220
Inflammation	1	533
Total Malignant	**14**	**23,220**
DCIS	1	194
IDC	12	22,547
ILC	1	479
Total Adipose	**9**	**7021**
Adipose	9	7021
Total ROI	**48**	**67,220**

were identified by the pathologist; these are summarized in Table 1. The pathologist identified seven tissue pathologies in the samples, which were classified more generally as not-malignant, malignant, or adipose.

Figure 2(a) illustrates coregistration between the white light image, histology, and images of scattering parameters for a tissue sample. Figures 2(b) and 2(c) show box plots of the scattering power and the logarithm of the wavelength-integrated irradiance with outliers removed (those of >2 standard deviations from the mean) for all tissue samples. The scattering amplitude is not displayed because it follows the same trend as the scattering power per diagnostic category, and a correlation is observed between the scattering power and the logarithm of the scattering amplitude [Fig. 2(d)].

Histopathology reveals that the three macroscopic scattering centers found in breast tissue are epithelia, stroma, and adipose. Immunohistochemistry shows that the percent distribution of these components varies with diagnosis, and registration of scattering maps with pathology illustrate how spectral response changes as a function of diagnosis. This suggests the percent distribution of stroma, epithelia and adipocytes in the effective illumination volume influences scattering response. Standard immunohistochemistry techniques were used to assess the percent distribution of adipose, stroma, and epithelia per sample. Formalin-fixed and paraffin-embedded tissue sections were cut and mounted on OptiPlus™ Positive Charged Barrier slides (BioGenex, San Ramon, California) to test for anti-cytokeratins 8 and 18 (clone 5D3; BioGenex, San Ramon, California). In brief, slides were deparaffinized with xylene and hydrated through graded alcohols, and epitope retrieval was carried out in a steamer under pressure. Slides were then rinsed in distilled water, soaked in phosphate-buffered saline, and immunostained using the BioGenex i6000™ Automated Staining System (San Ramon, California). Diaminobenzidine was applied for visualization, and hematoxylin was used as a counterstain. Slides were then dehydrated through graded alcohols and coverslips were applied. Whole immunostained slides were digitally scanned and montaged using the Surveyor® Automated Specimen Scanning (Objective Imaging Ltd., Cambridge, United Kingdom) automated stage control bundled software. The epithelia-to-stroma ratio was quantified using Image-Pro Plus (Media Cybernetics, Bethesda, Maryland) image-analysis software. The epithelial and stromal percentages were defined as the percent of CK5D3 positive or hematoxylin counterstained tissue, thresholded in pseudocolor in the diagnostic ROI, as compared to the total area of the tissue, respectively. Figure 3(a) shows fitted spectra sampled from normal, benign, and malignant tissues, respectively. Figure 3(b) illustrates how epithelia, stroma, and fat content vary between normal, benign, and malignant samples based on this analysis.

2.3 *k-NN Classification*

The distribution of scattering parameters demonstrated subtle discrimination between tissue subtypes, but data were multiparametric and overall classification was challenging. A *k*-NN classifier was employed for ready discrimination between tissue pathologies. The k-NN classifier simultaneously interprets multiple scattering parameters for tissue characterization by assigning an unclassified vector (herein referred to as the query point) to the majority diagnosis of its *k*-nearest vectors found in the feature space. The feature space for three scatter-related parameters (scattering amplitude, scattering power, and total wavelength-integrated intensity) is depicted in Fig. 2(d), as well as a query point with unknown diagnosis. All tissue pixels were defined according to a vector in the three-dimensional (3-D) feature space and were assigned to the training set (populated feature space) or to the validation set (query points). Sample distributions between training and validation sets were made both randomly and according to a leave-one-out analysis per patient.[45] All training pixels were associated with a known diagnosis according to the pathologist's demarcation of ROI. The diagnosis of each query point was also determined by the pathologist but remained unknown to the classifier in order to evaluate its performance.

Additional feature extraction from the actual data set has been shown to compensate for pixel-to-pixel variations and to improve the overall performance of the classifier.[6] Therefore, the first four statistical moments (mean, standard deviation, skewness, and kurtosis) of each scattering parameter were estimated in a real two-dimensional (2-D) spatial window centered about each pixel of interest. These local statistical parameters were concatenated to the actual scatter parameters, and parametric feature space was expanded from three-dimensions to 15 dimensions. The behavior of the classifier was then studied as a function of two independent variables: the number of nearest neighbors *k* and the size of the spatial window used to compute local statistics.

Accuracy of the *k*-NN classifier fundamentally depends on the metric used to compute distances between the query point and all training pixels in the feature space. To prevent some features from being more strongly weighted than others, data must be transformed so that all parameters are of the same order of magnitude. To standardize the dynamic range of the scattering parameters, scattering amplitude and average scatter irradiance were log-transformed. All scattering parameters

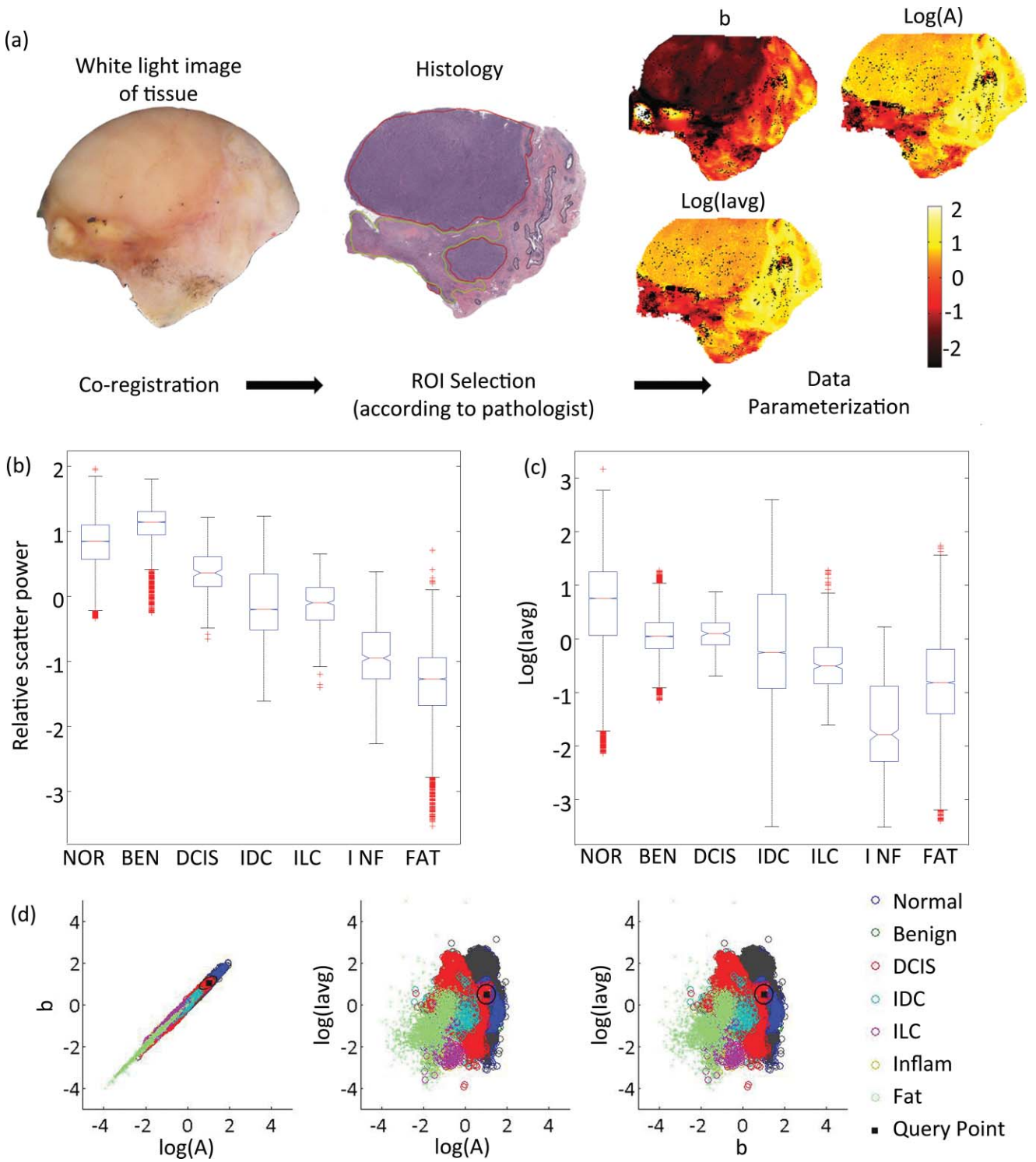

Fig. 2 (a) Coregistration between the digital photograph, histology, and maps of scattering power, amplitude, and total-wavelength integrated intensity for a given tissue sample; (b, c) box plots of relative scatter power and log of the total-wavelength integrated intensity according to diagnosis (outliers > 2 std not displayed) and (d) the 3-D feature space assembled with scattering parameters and employed by the *k*-NN classifier.

were statistically normalized to zero mean, and unit variance and outliers were removed from the feature space (training set) according to their interquartile fractions. Query points were never marked as outliers because this information would not be known *a priori*. When no prior knowledge is available about the probability density function of a particular class (diagnosis), most distance-based classifiers employ a Euclidean distance metric [Eq. (3)], where M is the identity matrix. The Euclidean metric assumes all parameters defining a pixel are equally important and independent of the others.[46]

$$d(x, y)^2 = (y - x)^T \mathrm{M}(y - x). \quad (3)$$

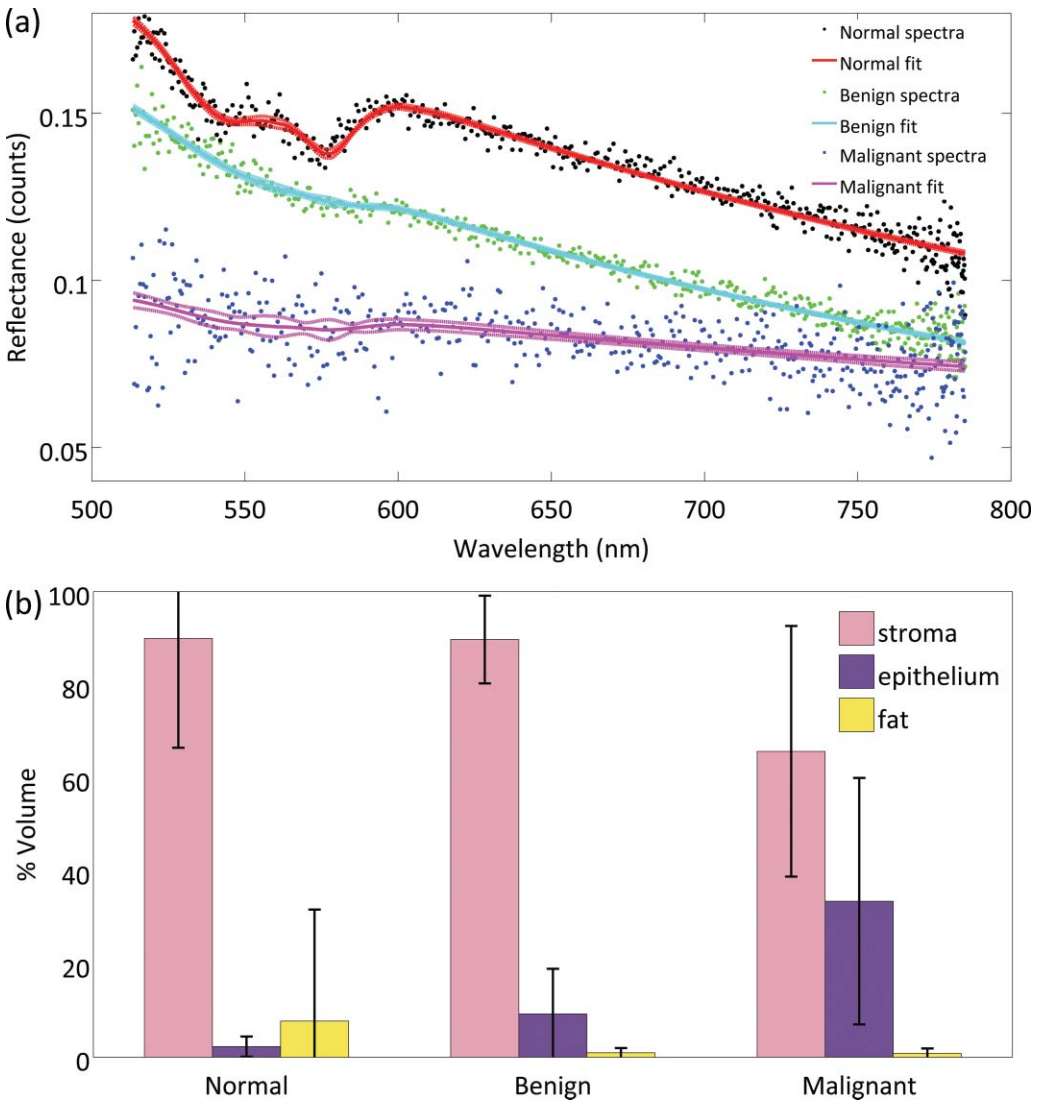

Fig. 3 (a) The fitted spectra sampled from normal, benign, and malignant tissues, respectively, are shown. (b) The distribution of stroma, epithelia and adipose are shown across the three diagnostic categories classified by immunohistochemistry for all tissue samples.

However, this metric is not ideal for this data set because evaluation of feature space reveals strong coupling between scattering amplitude and scattering power as evident in Fig. 2(d). Statistical regularities were estimated from a large training set and the Mahalanobis distance metric was employed to account for correlations between parameters. The Mahalanobis distance metric is given in Eq. (3), where M is the covariance matrix for the scattering parameters. In the special case where features are uncorrelated and variance is the same for all parameters, the Mahalanobis metric is equivalent to the Euclidean metric. A significant improvement in the *k*-NN classifier's performance was observed using the Mahalanobis metric as compared to the Euclidean metric for distance calculations with this data set.

2.4 *Validation of the Classifier*

In order to optimize the independent variables associated with the classifier, a threefold cross-validation technique was applied for discrimination between not-malignant, malignant, and adipose samples and for discrimination between all pathology subtypes identified in Table 1.[47,48] All data were randomly divided into three nonoverlapping sets, with an equal number of pixels per diagnostic category per set. Two of these sets were employed as a training set (used to populate feature space), and the other was employed as a validation set (query points) to compute the classification error. Error was taken to be the percentage of misclassified pixels in the validation set, where a misclassification means that the diagnosis assigned to a pixel by the automated classifier does not match the diagnosis provided by the pathologist. This procedure was repeated three times for all possible permutations of training and testing sets, and the reported classification error is the average of these three executions. This threefold cross-validation was repeated for a varying number of nearest neighbors, *k*, and a varying spatial window size for computation of local statistics.

Additionally, leave-one-out analysis was performed per patient, where ROI from one tissue sample populate the validation set and all other ROI pixels populate the feature space. In this validation procedure, points are not equally distributed between diagnostic categories in either the training or testing sets. Images of the classification results were generated in H&E false

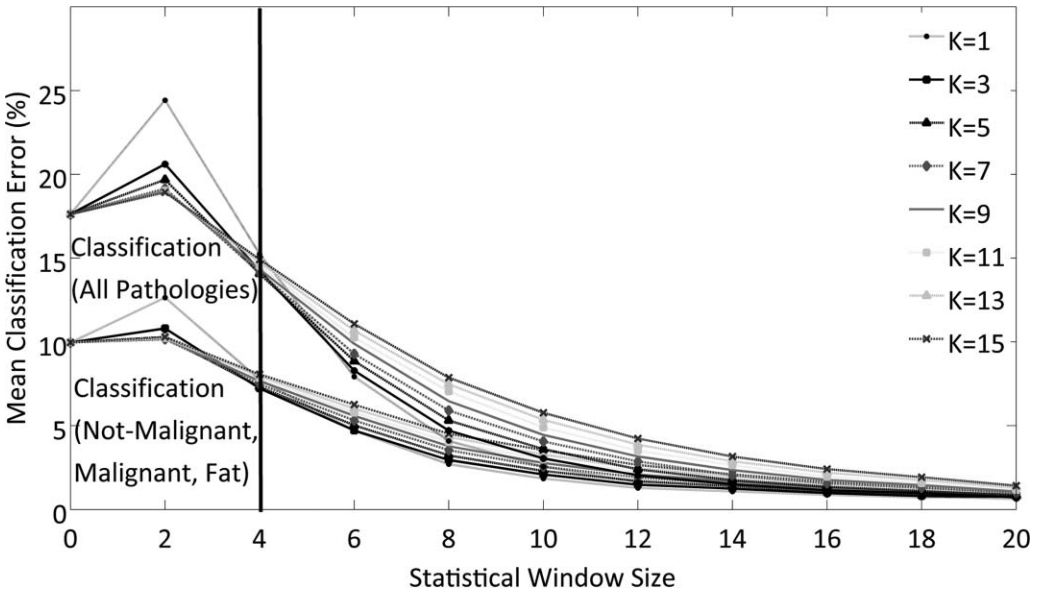

Fig. 4 Evaluation of *k*-NN classification error as a function of the number of nearest neighbors, *k*, and as a function of the local window size used to compute higher order statistics for discriminating between all pathologies and between not-malignant, malignant, and adipose pathologies.

color for each tissue sample, allowing one to evaluate whether the predicted diagnosis outside selected ROI makes sense in the context of the entire sample. A mode filter was applied in a sliding window (5×5 pixels) over the *k*-NN classified image to eliminate impulsive assignment noise. The error and efficacy of the classifier was summarized for all tissue samples.

Pixels corresponding to locations where reflectance spectra could not be reliably measured were tagged as masked pixels, and these were excluded from the training and validation sets during all cross-validation procedures.

3 Results

3.1 *Optimization of Independent Parameters in the Classifier*

Figure 4 depicts the behavior of the classification algorithm when discriminating between all pathologies (top lines on plot) and when discriminating more generally between not-malignant, malignant, and adipose tissues (bottom lines). Classification is repeated as a function of the spatial window used to compute local statistics and the number of *k*-NNs. Error is slightly higher when classifying all pathologies because the seven diagnostic categories identified by the pathologist are not equally represented with regard to the number of data points in feature space. Table 1 indicates that there are significantly more points in the feature space for the subtypes: normal epithelia and stroma, invasive ductal carcinoma (IDC), invasive lobular carcinoma (ILC), and adipose. The more general classification scheme was adopted to compensate for an uneven distribution of pixels per diagnostic category. The error asymptotically approaches ~2% for a decreasing number of nearest neighbors, *k*, and increasing spatial window for local statistics for both levels of classification. However, this accuracy is misleading and several features of the graph indicate that the classifier is governed by statistics rather than the actual scattering parameters when the spatial window for local statistics is >4 pixels (>400 μm). These indicators include the following:

1. As the spatial window for local statistics increases in size, the distributions used to compute local statistical parameters will become more normal and error should decrease; however, if the size of the window becomes too great, pixels from different diagnostic categories will be mixed and error will increase. Therefore, classification error should decrease with increasing spatial window size when the local window maintains separation between diagnostic categories. Because a consistent asymptotic decrease is observed in classification error for all evaluated local windows for statistics, the classifier is clearly governed by the statistical parameters for a large local window.
2. Classification accuracy is expected to increase with the number of nearest neighbors because this reduces the influence of outliers, rendering a diagnosis more probabilistic. This is observed when statistics are computed in a local window of <400 μm^2 surrounding the pixel of interest. For a larger local window, classification error increases with the number of nearest neighbors.

On the basis of these observations, a spatial window of 400 μm^2 was chosen to compute local statistical parameters and seven nearest neighbors were considered during automated diagnosis of pixels for the leave-one-out patient analysis. A 400 μm^2 window for computation of local statistics is physically reasonable because it approaches the mode of ROI dimensionality while preserving spatial resolution. These considerations were made so that the raw scattering parameters, not their statistics, govern the classifier's behavior. For 7-NN and a 400-μm^2 window for computation of local statistics, Fig. 4 approximates 14 and 8% error during leave-one-out analysis when discriminating between all pathologies and not-malignant, malignant, and adipose tissue, respectively.

Table 2 Summary of the classification error and total efficacy of the *k*-NN classifier when discriminating between not-malignant, malignant, and adipose tissue and when discriminating between all pathologies. Reported measures based on ability to discriminate given pathology from all other diagnostic categories evaluated.

	Classification (*Not-malignant, Malignant, Fat*)			Classification (All Pathologies)						
Classification Error										
Median	8.75			16.8						
Mean	13.0			25.3						
Standard Deviation	13.7			25.0						
Interquartile range	15.5			25.5						
[min max]	[0 53.5]			[2.15 95.3]						
Total Efficacy	Not-malignant	Malignant	Fat	Normal	Benign	DCIS	IDC	ILC	Inflam	Fat
Accuracy	0.86	0.86	0.98	0.74	0.85	1.00	0.86	0.99	0.99	0.98
Sensitivity	0.90	0.77	0.87	0.74	0.09	0.00	0.77	0.00	0.00	0.87
Specificity	0.82	0.90	0.99	0.74	0.91	1.00	0.90	1.00	1.00	0.99
Negative Predictive Value	0.87	0.88	0.99	0.77	0.92	1.00	0.89	0.99	0.99	0.99
Positive Predictive Value	0.86	0.81	0.95	0.71	0.08	0.00	0.79	0.00	0.00	0.95

3.2 *Discrimination between Tissue Pathologies per Sample*

Table 2 summarizes the classification efficacy and classification error observed when performing leave-one-out validation for all tissue samples. The median classification error is approximately 17 and 9% when discriminating between all pathologies and not-malignant, malignant, and adipose tissue, respectively. This is quite close to our performance estimates in Section 3.1. When classifying all pathologies, low sensitivity is observed for those classes under-represented in sample space (benign, DCIS, IDC, ILC, and inflammation). In any case, the classifier has clinical application because normal epithelia and stroma, IDC and adipose are the most frequently encountered tissues during conservative breast surgery. The classifier's sensitivity to not-malignant, malignant, and adipose pathologies is 0.90, 0.77, and 0.87, respectively. Sensitivity is lower in malignant samples because its sample population is characterized by greater heterogeneity. Although DCIS, IDC, and ILC are all considered malignant, morphologically and biologically they are quite distinct. Specificity of the classifier for not-malignant, malignant, and adipose pathologies is 0.82, 0.90, and 0.99, respectively. Specificity is lowest in normal tissues because these are characterized by mixed fibroglandular and adipose content. Epithelial proliferation in malignant tissues was observed to crowd out adipocytes in this study. In a reflectance geometry, scattering from adipocytes results in a very low (noisy) signal. The negative and positive predictive values for each diagnostic category are also reported. These refer to the number of patients with negative and positive results (respectively) who are correctly diagnosed. For surgical margin applications, the surgeon is most interested in a high negative predictive value, ensuring his/her diagnosis of normal or malignant is an accurate one. The negative predictive values for not-malignant and malignant pathologies are 87 and 88%, respectively. Although less essential, high positive predictive values prevent any unnecessary reexcisions during surgery.

The confusion matrices in Table 3 illustrate the distribution of misclassified pixels across diagnostic categories when performing leave-one-out analysis for two levels of diagnostic discrimination. This is important to consider because cost to the patient for misclassifying a normal pixel as benign is less than the cost to the patient for misclassifying a malignant pixel as normal.

Figure 5 illustrates classification of six representative tissue samples. The first column contains a digital photograph of each tissue sample taken immediately after spectral imaging; this is the surgeon's perspective. Fibroglandular tissue is white, adipose is yellow-orange, and higher concentrations of hemoglobin are red. Histological sections were coregistered to the scattering and white light images and are displayed in column 2. Hematoxylin has a deep blue-purple color and stains nucleic acids, which are primarily located in the cell nuclei. Eosin is pink and stains proteins nonspecifically; mainly, the cytoplasm and stroma have varying degrees of pink staining. Fat is not preserved during histological processing; thus, this becomes empty space on the slide. Column 3 illustrates the ROI identified by the pathologist, and they are colored according to their true diagnostic category, while column 4 contains images of the automated diagnosis provided by the *k*-NN classifier.

Table 3 (a) A confusion matrix, under leave-one-out validation, that represents trends in misclassification and accurate identification of benign and malignant pathologies. (b) A confusion matrix, under leave-one-out validation, that represents trends in misclassification and accurate identification of all pathologies identified by WAW. The matrices list the percentage of pixels classified correctly along the diagonal (gray), and incorrectly off of the diagonal. Clear misclassifications are highlighted in bold.

(a)

ESTIMATED DIAGNOSIS \ TRUE DIAGNOSIS	Benign	Malignant
Benign	90.8%	23.1%
Malignant	9.2%	76.9%
TOTAL # DIAGNOSED PIXELS	44,000	23,220

(b)

ESTIMATED DIAGNOSIS \ TRUE DIAGNOSIS	Normal	Benign	DCIS	IDC	ILC	Inflam	Fat
Normal	73.8%	**85.2%**	**83.0%**	20.0%	21.3%	3.8%	1.1%
Benign	16.6%	9.2%	8.8%	1.7%	1.3%	0.0%	0.3%
DCIS	0.0%	0.0%	0.0%	0.0%	0.0%	0.0%	0.0%
IDC	9.3%	5.5%	7.2%	77.4%	**73.5%**	**68.1%**	9.3%
ILC	0.0%	0.0%	0.0%	0.2%	0.0%	3.4%	0.4%
Inflam	0.0%	0.0%	0.0%	0.1%	1.3%	0.0%	1.6%
Fat	0.3%	1.0%	1.0%	0.5%	2.7%	24.8%	87.3%
TOTAL # DIAGNOSED PIXELS	31226	5220	194	22547	479	533	7021

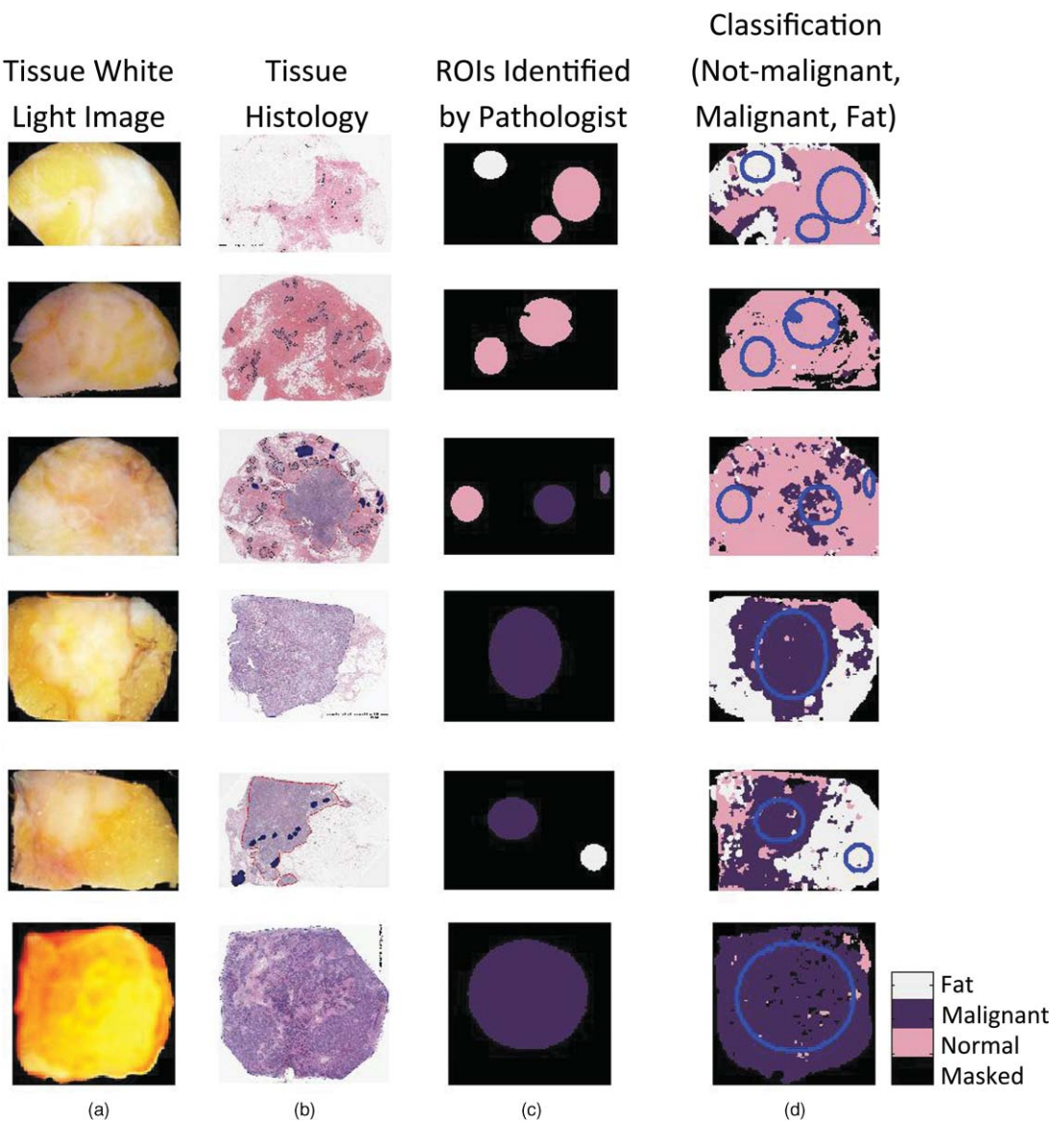

Fig. 5 Classification of six representative tissue samples. Each row corresponds to a different tissue sample, and the following four images are co-registered: (a) a white light image of the tissue, (b) H&E stained section of tissue, (c) true diagnosis of ROI identified by the pathologist (WAW), and (d) classification results when discriminating between not-malignant, malignant, and adipose tissues.

We recognize that the surgeon is most interested in a diagnosis of either benign or malignant; therefore, the *k*-NN classifier was executed with this binary level of discrimination. When separating benign and malignant pathologies, the sensitivity and specificity was 91 and 77%, respectively, and the system achieved positive and negative predictive values of 88 and 81%, respectively.

4 Discussion

This study demonstrates that morphological features pertinent to a tissue's diagnosis may be ascertained from confocal detection of broadband reflectance, with a mesoscopic resolution that permits scanning of an entire margin for residual disease. The technical aspects and optimization of a *k*-NN classifier for automated diagnosis of pathologies is presented and validated in 29 specimens of breast tissue. The classifier's discriminating capabilities improved with the inclusion of local statistics, likely accounting for microscopic tissue heterogeneities. Initially, discrimination between all pathologies identified by WAW was attempted; however, inadequate sampling of uncommon pathologies rendered their classification less robust. Given the sample population, discrimination between not-malignant, malignant, and adipose pathologies was most intuitive; particularly because these diagnostic categories correspond to the three macroscopic scattering centers in breast tissue (stroma, epithelia and adipocytes). Negative predict values of 87, 88, and 99% were achieved for not-malignant, malignant, and adipose tissues, respectively. In the same order, their positive predictive values were 86, 81, and 95%. The classifier was most sensitive to not-malignant and adipose tissues because the malignant population was pathologically very diverse; including samples of ILC, IDC, and DCIS. Specificity was lowest in not-malignant samples because of their mixed fibroglandular and adipose content. In the context of conservative surgery, the goal of treatment is to maximize removal of malignant tissues while minimizing damage to healthy, viable tissue. When discriminating between benign and malignant tissues only, a sensitivity of 91% and a specificity of 77% was achieved. This sensitivity is significantly higher than those reported for frozen section analysis (which is not practical for lumpectomy margins because of the problems associated with freezing and cutting adipose tissues) and diffuse reflectance spectroscopy, although its specificity is lower.[23,49,50] Even though overall efficacy of the classifier exceeds or is comparable to other intraoperative assessment techniques, integration of spectroscopy methods into the surgical suite will require a better negative predictive value, ensuring that the surgeon's diagnosis of benign or malignant is an accurate one. Additionally, higher positive predictive values would prevent unnecessary tissue removal during surgery. Efficacy of the proposed technique may be enhanced with better or more data and further optimization of the classifier itself.

This is a very purposeful application of spectroscopy because it uses optical measures as defined according to pathology criteria and may inform clinical practice during surgery. While mechanically scanning the sample was time intensive and therefore not suitable for clinical translation. A second-generation system is under development that employs a scanning-beam architecture to image tissue fields up to 1.5×1.5 cm^2 within 2–3 min. The combination of tissue spectroscopy with automated classification may provide information about tissue morphology, intraoperatively, so that if residual tumor is present at one or more margins, then the surgeon (before closing) could be advised to remove more tissue immediately—rather than at a later reexcision. Additionally, wide-field optical maps generated by the system may guide sampling of pathology by highlight suspicious lesions for more detailed investigation. Particularly, the greatest potential clinical impact could be intraoperative detection of DCIS, which has a very important status in breast pathology because its presence is a powerful predictor for local disease reoccurrence and its identification during surgery influences treatment options.[51–54] DCIS is a nonpalpable lesion, unidentifiable during surgery; consequently, characterization of its spectral response could dramatically improve patient care. Finally, understanding the relationship between the optical and biological properties of a tissue will ultimately improve the diagnostic utility of optical techniques, permitting optimization of the measurement procedure and signal analysis for enhanced sensitivity to differentiating features. The technique remains to be tested intraoperatively. Future clinical studies will reveal how the system may enhance existing surgery and pathologic procedures.

One lesson learned over the course of this study was that reflectance measures from tissues with high adipose content were characteristically low (and noisy). Our proposed technological solution is automation of a variable integration time, permitting longer data collection at points with a low signal until a minimum number of photons are detected. Scrutiny of classified tissue samples revealed that the greatest number of masked pixels (a consequence of poor data fit to the empirical model) were found in regions of high adipose content, and misclassification frequently occurred in regions of mixed fibroglandular and adipose content. Garcia-Allende et al.[6] achieved nearly perfect sensitivity and specificity when classifying tissue subtypes in pancreas tumors, mainly because pancreas tissue is highly stromal and almost completely lacking adipose content. Additionally, note that trends in scattering parameters are inverted regarding diagnosis in the breast as compared to the pancreas. This is because malignancy is essentially stromal in the pancreas and epithelial in the breast, and the percent distribution of stroma, epithelia and adipocytes in the interrogation volume fundamentally influences the scattered signal there.

Preliminary analysis of parameter covariance reveals a correlation between the logarithm of the relative scattering amplitude and scattering power. This correlation was also observed in a previous study analyzing the scattering response of pancreas tissue,[56] suggesting that the discriminating ability of the relative scattering amplitude and power may be the same. In this work, they were treated independently during classification and a Mahalanobis distance metric was employed so that classifier efficacy was not influenced by their likeness in value. The biological underpinnings of this correlation are not yet clear and beyond the scope of this paper. However, extracting independent information from the relative scattering amplitude and power will be an important focus of controlled phantom experimentation.

To expand on the variety of data collected, a new scanning spectroscopy imaging system is being developed to allow broadband spectral imaging of breast pathology in a waveband (400–700 nm) that is sensitive to both tissue morphology and biochemical composition. Particularly, within this

waveband one may determine the concentration of oxygenated and deoxygenated hemoglobin, beta carotene, and blood breakdown products in a tissue, while simultaneously extracting scattering features in a region with minimal absorption (>620 nm). Addition of other optical parameters to the classifier is extremely simple, only involving an expansion of feature space (update the vector describing each pixel to N dimensions, where N is the number of parameters). It would be particularly useful to generate a comprehensive dataset with parameters describing all possible endogenous light–tissue interactions (scattering, absorption, fluorescence), so that the most diagnostically discriminating and robust parameters could be identified and optimized during data collection. Note that beta-carotene is a member of the carotenoids and gives fat its highly pigmented, yellow color; we hope that its absorption spectra will improve classification of tissues with high adipose content. Finally, to enhance the specificity of spectroscopic diagnosis, one could envision the use of Raman spectroscopy in suspicious regions identified by broadband reflectance. Nucleic acids, proteins, and lipids have distinct Raman features that provide highly specific structural and environmental information; its primary limitation has always been sensitivity.[18]

Improvement of the classifier's performance may fundamentally be achieved with greater sampling. As the number of data points in feature space increases, so does the accuracy of the classifier.[55] Particularly, the classifier's sensitivity to malignant pathologies has the most to gain and could be improved with equal representation of IDC, ILC, and DCIS in feature space. As feature space expands, so will computational costs. Rather than calculating the distance between each query point and every point in feature space, a k-dimensional tree may be employed to optimize the search algorithm.[56] The classifier was trained with ROI obviously belonging to a diagnosis; normal and malignant pathologies were identified by cellular features in fibroglandular regions and adipose ROI were measured far from any fibroglandular tissue. Perhaps the performance of the classifier would improve if an additional level of classification was employed, so that each diagnostic category was also labeled according to the subtypes, "fibroglandular" or "fattyfibroglandular."

5 Conclusions

In this contribution, we validate and optimize the ability of a k-NN classifier to automatically detect breast tissue pathologies based on direct sampling of elastic scattering features. The sampling volume was specifically chosen to be sensitive to architectural changes addressed by a pathologist during microscopic assessment of a surgical specimen, while also permitting its wide-field scanning. Performance of the classifier was assessed in 29 breast tissue specimens, and when discriminating between benign and malignant pathologies, a sensitivity and specificity of 91 and 77% was achieved. Furthermore, detailed subtissue analysis was performed to consider how diverse pathologies influence scattering response and overall classification efficacy. Classification efficacy was influenced by the number of samples used in training, the level of discrimination used in separating tissue types, as well as morphological features inherent to each pathology. The increased sensitivity of this technique may render it useful to guide the surgeon where to look when evaluating an involved surgical margin or the pathologist where to sample a gross specimen for microscopic assessment. We expect that specificity and overall classification efficacy will improve with the inclusion of additional optical parameters, such as absorption and fluorescence because these are responsive to the tissue's biochemical state.

Acknowledgments

This work was funded by National Institute of Health Grant No. PO1 CA80139 and the DoD CDMRP Grant No. BC093811. The authors also acknowledge the technical expertise of Mary Schwab and Rebecca O'Meara in the Department of Pathology at DHMC for their help with immunohistochemistry and histology.

References

1. F. Fitzal, O. Riedl and R. Jakesz, "Recent developments in breast-conserving surgery for breast cancer patients," *Langenbeck's Archives of Surgery* **394**(4), 591-609 (2009).
2. R. Pleijhuis, M. Graafland, J. de Vries, J. Bart, J. de Jong and G. van Dam, "Obtaining Adequate Surgical Margins in Breast-Conserving Therapy for Patients with Early-Stage Breast Cancer: Current Modalities and Future Directions," *Annals of Surgical Oncology* **16**(10), 2717-2730 (2009).
3. C. Rogers, E. C. Klatt and P. Chandrasoma, "Accuracy of Frozen-Section Diagnosis in a Teaching Hospital," *Archives of Pathology & Laboratory Medicine* **111**(6), 514-517 (1987).
4. R. Laucirica, "Intraoperative assessment of the breast - Guidelines and potential pitfalls," *Archives of Pathology & Laboratory Medicine* **129**(12), 1565-1574 (2005).
5. V. Krishnaswamy, P. J. Hoopes, K. S. Samkoe, J. A. O'Hara, T. Hasan and B. W. Pogue, "Quantitative imaging of scattering changes associated with epithelial proliferation, necrosis, and fibrosis in tumors using microsampling reflectance spectroscopy," *J. Biomed. opt.* **14**(1), 014004 (2009).
6. P. B. Garcia-Allende, V. Krishnaswamy, P. J. Hoopes, K. S. Samkoe, O. M. Conde and B. W. Pogue, "Automated identification of tumor microscopic morphology based on macroscopically measured scatter signatures," *J. Biomed. opt.* **14**(3), 034034 (2009).
7. V. Backman, et al., "Measuring cellular structure at submicrometer scale with light scattering spectroscopy," *IEEE Journal of Selected Topics in Quantum Electronics* **7**(6), 887-893 (2001).
8. L. T. Perelman, et al., "Observation of periodic fine structure in reflectance from biological tissue: A new technique for measuring nuclear size distribution," *Physical Review Letters* **80**(3), 627-630 (1998).
9. C. D. Scopa, P. Aroukatos, A. C. Tsamandas and C. Aletra, "Evaluation of Margin Status in Lumpectomy Specimens and Residual Breast Carcinoma," *The Breast Journal* **12**(2), 150-153 (2006).
10. M. C. Smitt, K. W. Nowels, M. J. Zdeblick, S. Jeffrey, R. W. Carlson, F. E. Stockdale and D. R. Goffinet, "The Importance of the Lumpectomy Surgical Margin Status in Long-Term Results of Breast-Conservation," *Cancer* **76**(2), 259-267 (1995).
11. B. Spivack, M. M. Khanna, L. Tafra, G. Juillard and A. E. Giuliano, "Margin Status and Local Recurrence after Breast-Conserving Surgery," *Arch Surg-Chicago* **129**(9), 952-956 (1994).
12. S. J. Schnitt, J. R. Harris and B. L. Smith, "Developing a prognostic index for ductal carcinoma in situ of the breast - Are we there yet?," *Cancer* **77**(11), 2189-2192 (1996).
13. D. E. Wazer, T. Dipetrillo, R. Schmidtullrich, L. Weld, T. J. Smith, D. J. Marchant and N. J. Robert, "Factors Influencing Cosmetic Outcome and Complication Risk after Conservative Surgery and Radiotherapy for Early-Stage Breast-Carcinoma," *J Clin Oncol* **10**(3), 356-363 (1992).
14. I. A. Olivotto, M. A. Rose, R. T. Osteen, S. Love, B. Cady, B. Silver, A. Recht and J. R. Harris, "Late Cosmetic Outcome after Conservative Surgery and Radiotherapy - Analysis of Causes of Cosmetic Failure," *Int J Radiat Oncol* **17**(4), 747-753 (1989).
15. G. C. Balch, S. K. Mithani, J. F. Simpson and M. C. Kelley, "Accuracy of Intraoperative Gross Examination of Surgical Margin Status in Women Undergoing Partial Mastectomy for Breast Malignancy," *American Surgeon* **71**(1), 22-28 (2005).

16. M. R. Wick and S. E. Mills, "Evaluation of surgical margins in anatomic pathology: Technical, conceptual, and clinical considerations," *Semin Diagn Pathol* **19**(4), 207-218 (2002).
17. M. R. Austwick, et al., "Scanning elastic scattering spectroscopy detects metastatic breast cancer in sentinel lymph nodes," *J. Biomed. Opt.* **15**(4), 047001 (2010).
18. A. Mahadevan-Jansen, M. F. Mitchell, N. Ramanujam, A. Malpica, S. Thomsen, U. Utzinger and R. Richards-Kortum, "Near-infrared Raman spectroscopy for in vitro detection of cervical precancers," *Photochem Photobiol* **68**(1), 123-132 (1998).
19. C. J. Frank, R. L. McCreery and D. C. B. Redd, "Raman-spectroscopy of normal and diseased human breast tissues," *Anal Chem* **67**(5), 777-783 (1995).
20. I. J. Bigio, et al., "Diagnosis of breast cancer using elastic-scattering spectroscopy: preliminary clinical results," *J. Biomed. Opt.* **5**(2), 221-228 (2000).
21. I. J. Bigio and J. R. Mourant, "Ultraviolet and visible spectroscopies for tissue diagnostics: Fluorescence spectroscopy and elastic-scattering spectroscopy," *Phys. Med. Biol.* **42**(5), 803-814 (1997).
22. A. C. Lee, C. D. O. Pickard, M. R. S. Keshtgar, G. M. Briggs, M. Falzon, S. Lakhani, I. Bigio and S. G. Bown, "Elastic scattering spectroscopy for the diagnosis of breast cancer," *Brit J Surg* **89**, 74-74 (2002).
23. T. M. Breslin, G. Palmer, C. Fang, K. W. Gilchrist, F. Xu and N. Ramanujam, "Auto fluorescence and diffuse reflectance properties of malignant and benign breast tissues," *Annals of Surgical Oncology* **10**(1), S16-S16 (2003).
24. V. Backman, et al., "Detection of preinvasive cancer cells," *Nature* **406**(6791), 35-36 (2000).
25. I. Georgakoudi, "The color of cancer," *J Lumin* **119**, 75-83 (2006).
26. I. Georgakoudi, et al., "Fluorescence, reflectance, and light-scattering spectroscopy for evaluating dysplasia in patients with Barrett's esophagus," *Gastroenterology* **120**(7), 1620-1629 (2001).
27. I. Georgakoudi, E. E. Sheets, M. G. Muller, V. Backman, C. P. Crum, K. Badizadegan, R. R. Dasari and M. S. Feld, "Trimodal spectroscopy for the detection and characterization of cervical precancers in vivo," *Am J Obstet Gynecol* **186**(3), 374-382 (2002).
28. M. G. Muller, et al., "Spectroscopic detection and evaluation of morphologic and biochemical changes in early human oral carcinoma," *Cancer* **97**(7), 1681-1692 (2003).
29. M. D. Keller, S. K. Majumder, M. C. Kelley, I. M. Meszoely, F. I. Boulos, G. M. Olivares and A. Mahadevan-Jansen, "Autofluorescence and diffuse reflectance spectroscopy and spectral imaging for breast surgical margin analysis," *Lasers in Surgery and Medicine* **42**(1), 15-23 (2010).
30. T. M. Breslin, F. S. Xu, G. M. Palmer, C. F. Zhu, K. W. Gilchrist and N. Ramanujam, "Autofluorescence and diffuse reflectance properties of malignant and benign breast tissues," *Annals of Surgical Oncology* **11**(1), 65-70 (2004).
31. G. M. Palmer, P. J. Keely, T. M. Breslin, K. W. Gilchrist and N. Ramanujam, "Ex vivo diagnosis of breast cancer using fluorescence and reflectance spectroscopy," *Lasers in Surgery and Medicine National Meeting (Atlanta, GA)*, 76-76 (2002).
32. C. Zhu, G. M. Palmer, T. M. Breslin, J. Harter and N. Ramanujam, "Diagnosis of breast cancer using fluorescence and diffuse reflectance spectroscopy: a Monte-Carlo-model-based approach," *J. Biomed. Opt.* **13**(3), 034015 (2008).
33. L. G. Wilke, et al., "Rapid noninvasive optical imaging of tissue composition in breast tumor margins," *Am J Surg* **198**(4), 566-574 (2009).
34. A. Amelink and H. Sterenborg, "Measurement of the local optical properties of turbid media by differential path-length spectroscopy," *Applied Optics* **43**(15), 3048-3054 (2004).
35. A. Amelink, H. Sterenborg, M. P. L. Bard and S. A. Burgers, "In vivo measurement of the local optical properties of tissue by use of differential path-length spectroscopy," *Optics Letters* **29**(10), 1087-1089 (2004).
36. R. L. P. van Veen, A. Amelink, M. Menke-Pluymers, C. Van Der Pol and H. J. C. M. Sterenborg, "Optical biopsy of breast tissue using differential path-length spectroscopy," *Phys. Med. Biol.* **50**(11), 2573-2581 (2005).
37. B. W. Pogue and T. Hasan, "Fluorophore quantitation in tissue-simulating media with confocal detection," *IEEE Journal of Selected Topics in Quantum Electronics* **2**(4), 959-964 (1996).
38. B. W. Pogue and G. Burke, "Fiber-optic bundle design for quantitative fluorescence measurement from tissue," *Applied Optics* **37**(31), 7429-7436 (1998).
39. J. R. Mourant, J. P. Freyer, A. H. Hielscher, A. A. Eick, D. Shen and T. M. Johnson, "Mechanisms of light scattering from biological cells relevant to noninvasive optical-tissue diagnostics," *Applied Optics* **37**(16), 3586-3593 (1998).
40. H. J. Vanstaveren, C. J. M. Moes, J. Vanmarle, S. A. Prahl and M. J. C. Vangemert, "Light-Scattering in Intralipid-10-Percent in the Wavelength Range of 400-1100 Nm," *Applied Optics* **30**(31), 4507-4514 (1991).
41. M. Bartek, X. Wang, W. Wells, K. D. Paulsen and B. W. Pogue, "Estimation of subcellular particle size histograms with electron microscopy for prediction of optical scattering in breast tissue," *J. Biomed. Opt.* **11**(6), 064007 (2006).
42. X. Wang, et al., "Image reconstruction of effective Mie scattering parameters of breast tissue in vivo with near-infrared tomography," *J. Biomed. Opt.* **11**(4), 041106 (2006).
43. X. Wang, B. W. Pogue, S. D. Jiang, X. M. Song, K. D. Paulsen, C. Kogel, S. P. Poplack and W. A. Wells, "Approximation of Mie scattering parameters in near-infrared tomography of normal breast tissue in vivo," *J. Biomed. Opt.* **10**(5), 051704 (2005).
44. S. L. Jacques, Prahl, S., "Optical Properties Spectra" (Oregon Medical Laser Center, Portland, OR, 2010), http://omlc.ogi.edu/.
45. O. Eytan, B. A. Sela and A. Katzir, "Fiber-optic evanescent-wave spectroscopy and neural networks: application to chemical blood analysis," *Applied Optics* **39**(19), 3357-3360 (2000).
46. D. A. Burns, Ciurczak, E.W., "Qualitative Discriminant Analysis," *Handbook of Near-Infrared Analysis* (Chpt. 15), 3rd ed. (CRC Press, 2008).
47. C. Goutte, "Note on free lunches and cross-validation," *Neural Comput* **9**(6), 1245-1249 (1997).
48. H. Y. Zhu and R. Rohwer, "No free lunch for cross-validation," *Neural Comput* **8**(7), 1421-1426 (1996).
49. N. Cabioglu, et al., "Role for Intraoperative Margin Assessment in Patients Undergoing Breast-Conserving Surgery," *Annals of Surgical Oncology* **14**(4), 1458-1471 (2007).
50. G. M. Palmer, C. F. Zhu, T. M. Breslin, F. S. Xu, K. W. Gilchrist and N. Ramanujam, "Comparison of multiexcitation fluorescence and diffuse reflectance spectroscopy for the diagnosis of breast cancer (March 2003)," *IEEE T Bio-Med Eng* **50**(11), 1233-1242 (2003).
51. N. Q. Mirza, et al., "Ductal carcinoma-in-situ: Long-term results of breast-conserving therapy," *Annals of Surgical Oncology* **7**(9), 656-664 (2000).
52. E. B. Claus, S. Petruzella, E. Matloff and D. Carter, "Prevalence of BRCA1 and BRCA2 mutations in women diagnosed with ductal carcinoma in situ," *JAMA-Journal of the American Medical Association* **293**(8), 964-969 (2005).
53. N. S. Goldstein, L. Kestin and F. Vicini, "Intraductal carcinoma of the breast - Pathologic features associated with local recurrence in patients treated with breast-conserving therapy," *American Journal of Surgical Pathology* **24**(8), 1058-1067 (2000).
54. M. R. Bani, M. P. Lux, K. Heusinger, E. Wenkel, A. Magener, R. Schulz-Wendtland, M. W. Beckmann and P. A. Fasching, "Factors correlating with reexcision after breast-conserving therapy," *European Jounral of Surgical Oncology* **35**(1), 32-37 (2009).
55. P. B. Garcia-Allende et al., "Automated identification of tumor microscopic morphology based on microscopically measured scatter signatures," *J. Biomed. Opt.* **14**(3), 034034 (2009).
56. K. Fukunaga, *Introduction to Statistical Pattern Recognition*. (Academic Press, New York, 1972).